ARTICLE

OPEN

Quantum dot activated indium gallium nitride on silicon as photoanode for solar hydrogen generation

Praveen Kumar[1], Pooja Devi[2], Rishabh Jain [2], S.M. Shivaprasad[3], R.K. Sinha[2], Guofu Zhou[4] & Richard Nötzel[4]

Nitride alloys are considered potential candidates as photoelectrodes for photoelectrochemical water splitting. Here we show an $In_{0.25}Ga_{0.75}N$ layer activated by indium nitride quantum dots as efficient photoanode for photoelectrochemical hydrogen generation by water splitting when directly grown on cheap silicon (111) substrates. Photocurrent measurements show more than five times enhancement by the indium nitride quantum dots compared to a bare $In_{0.25}Ga_{0.75}N$-on-silicon photoanode. The maximum incident photon-to-current conversion efficiency is 44% at 550 nm at 0.4 V, the applied-bias photon-to-current efficiency is 4.1% and the hydrogen and oxygen generation rates are 75 $\mu mol\, h^{-1}\, cm^{-2}$ and 33 $\mu mol\, h^{-1}\, cm^{-2}$ at 0.2 V under 100 mW cm^{-2} white light illumination.

[1] School of Materials Sciences, Indian Association for the Cultivation of Science, Kolkata 700030, India. [2] CSIR-Central Scientific Instruments Organisation, Sector-30C, Chandigarh 160030, India. [3] Jawaharlal Nehru Centre for Advanced Scientific Research, Bangalore 560064, India. [4] South China Normal University, Academy of Advanced Optoelectronics, Guangzhou 510006, China. Correspondence and requests for materials should be addressed to P.K. (email: praveen.kumar@iacs.res.in) or to P.D. (email: poojaiitr@csio.res.in)

Owing to the worldwide deficit in the supply of fossil fuel, the search for sustainable alternative energy sources has become an important area of research[1,2]. Solar-driven artificial photosynthesis to produce hydrogen by photoelectrochemical (PEC) water splitting using semiconductor photoelectrodes offers a clean, environmentally friendly solution and is considered as one of the most promising techniques to sustain the global energy supply[3–5]. After the first experiments by Fujishima and Honda, various semiconductor materials were investigated in search for highly efficient, stable and cost-effective photoelectrodes[6–8]. The main focus was on metal oxides with TiO_2 as the most favoured anode material[9,10]. However, due to the large band gap energy (3.2 eV) and, hence, low absorption of solar radiation (<3%) the efficiency of PEC hydrogen generation by TiO_2 is low (<2%)[11].

Recently, the highest efficiencies above 10% were reported using tandem III–V semiconductor structures (solar cells plus photoelectrodes), but their complexity is high and their stability against photocorrosion is not sufficient[12,13]. Regarding the choice of materials for photoelectrodes, InGaN ternary alloys are of great interest due their band gap tuning across the entire visible spectrum, straddling band alignment with the O_2/H_2O and H^+/H_2 water oxidation and reduction potentials, high absorption coefficient and high corrosion resistance[14–16]. Furthermore, InN has been identified as a potential electrocatalyst for ZnO photoelectrodes[17]. Most of the reported III-nitrides based photoelectrodes were fabricated employing buffer layers of GaN/AlN and foreign (co-) catalyst coupling on the surface, which causes the development of these photoelectrodes far beyond commercially viable cost[18,19].

Therefore, efforts are now to produce these high-quality III-nitrides based photoelectrodes directly on Si substrates, however, with limited success due to large lattice and thermal expansion mismatch and compositional phase separation, leading to non-radiative defects and poor carrier transport. Due to the difficulties in growing high-quality high-Indium content InGaN layers on Si, efforts have been made to grow InGaN-based nanostructures and explore them as photoelectrodes for water splitting[20–22]. There are only a few studies of these InGaN-based photoelectrodes on Si and they report modest efficiencies below 1%. Therefore, to achieve the ultimate goal of device fabrication, it is highly desirable to grow such photoelectrodes directly on Si substrates without degradation of performance and in the absence of buffer layers or foreign (co-) catalysts for ultimate cost reduction. This is a major challenge and to the best of our knowledge such a photoelectrode has not been demonstrated yet; presumably due to the difficulties in growing high-quality InGaN layers directly on Si substrates.

Here we show the optimized growth of $In_{0.25}Ga_{0.75}N$ layers directly on Si (111), followed by their surface activation with InN quantum dots (QDs). InGaN layers are obtained on the nitrided surface of the Si substrate by careful adjustment of the growth temperature and N-to-In + Ga flux ratio. Furthermore, we study the PEC properties of the InN-QDs/$In_{0.25}Ga_{0.75}N$-layer/Si photoanode (denoted photoanode A) in comparison to a bare $In_{0.25}Ga_{0.75}N$-layer/Si photoanode (denoted photoanode B) for solar-driven hydrogen generation by water splitting. The activated photoanode shows more than five times enhanced PEC efficiency with a hydrogen production rate of ~ 75 μmol h^{-1} cm^{-2} at 0.2 V under 100 mW cm^{-2} white light illumination. This is a major step toward our goal of realizing highly efficient photoanodes grown directly on Si without using any buffer layers or foreign (co-)catalysts to reduce the overall cost, benefiting from the mature Si technology.

Results

Morphological and structural properties. Figure 1 depicts the morphological (field-emission scanning electron microscopy (FE-SEM) and atomic force microscopy (AFM)) and structural (high-resolution X-ray diffraction (HRXRD) $\omega-2\theta$ scans recorded in the vicinity of the Si (111) and InGaN (0002) Bragg reflections) data of the InGaN plus InN QDs (photoanode A) and bare InGaN layer (photoanode B). The top-view SEM images of photoanodes (A and B) are shown in Fig. 1a, b, whereas the cross-sectional image of photoanode B is shown in Fig. 1c, which confirms the grown layer thickness of 450 nm. The HRXRD spectra of photoanodes A (blue) and B (black) are shown in Fig. 1d. The peaks centered at 14.22° and 16.86° correspond to the symmetric Si (111) and $In_{0.25}Ga_{0.75}N$ (0002) Bragg reflections, respectively. The narrow and symmetric XRD diffraction peaks of the InGaN layers with ~0.28° full-width at half-maximum (FWHM) reveal good crystal quality of the InGaN layers without marked compositional phase separation. The In content was determined using Vegard's law by linear interpolation between the peak positions of GaN and InN. Full reciprocal space mapping has shown complete relaxation of the InGaN layers[23]. To clearly resolve the InN QDs, AFM images are shown in Fig. 1e with different scales. The height of the QDs is 3–4 nm, the diameter is 30–40 nm and the density is about 1.5×10^8 cm^{-2}.

Optical and electrical properties. The optical and electrical properties of the photoanodes were probed by low-temperature photoluminescence (LT-PL) spectroscopy and current-voltage (I–V) measurements, shown in Fig. 2. A He–Cd laser (325 nm wavelength, 10 W cm^{-2} power density) was used as excitation source for the LT-PL measurements of the InGaN layers, whereas a laser diode (781 nm peak wavelength, 300 mW excitation power) was used as excitation source for measuring the InN QDs. The LT-PL spectra in Fig. 2a clearly indicate the good optical properties of the InGaN layers of photoanodes A (blue) and B (black) with a single emission peak centered at 2.15 eV. The relatively large line width (FWHM ~0.16 eV) is due to residual composition fluctuations[24]. The corresponding band gap energy of 2.15 eV is well suited for PEC water splitting. The inset in Fig. 2a shows the PL emission from the InN QDs of photoanode A in the near-infrared region, centered at 1.05 eV. This emission energy is in reasonable agreement with the QD size, considering only quantum confinement due to the QD height. Two-probe top-to-top I–V measurements for both photoanodes were performed to confirm the ohmic behavior of the electrical top contacts employed for the PEC measurements. The I–V curves of photoanodes A (blue) and B (black) shown in Fig. 2b are close to linear. The inset depicts a scheme of the sample structure, Al contacts and measurement setup. The high n-type conductivity of the InGaN layers is due to defects acting as donors.

Near-surface electronic properties. The electronic behavior of the photoanodes was probed by X-ray photoelectron spectroscopy (XPS) (Supplementary Note 1). The deconvoluted core level spectra are presented in Supplementary Fig. 1. The valence band (VB) spectra of photoanodes A and B shown in Fig. 3a, b, respectively, were recorded to measure the near-surface band bending, which is crucial for the PEC performance. Two samples of each photoanode were analyzed to minimize effects of surface contamination and an average of 12 spectra was taken for evaluation. Carbon correction was done for all photoanodes by shifting the XPS VB spectra with respect to the free carbon (C-C) related peak at 284.6 eV, to eliminate charging effects[25]. The VB spectra provide information about the occupied electron states close to the surface. The binding energy of the occupied electron states is the energy relative to the Fermi energy where the binding energy is zero. Therefore, the energy difference between the valence band edge at the surface and the surface Fermi energy,

$E_{VS} - E_{FS}$, is given by the onset of the intensity, determined by extrapolating the VB spectra. The $E_{VS} - E_{FS}$ values are 1.85 and 1.65 eV for photoanodes A and B, respectively. As the Fermi energy in the bulk of the highly n-type InGaN layer is close to the conduction band edge, this means upward band bending close to the surface with a barrier height of 0.05 and 0.25 eV for photoanodes A and B, respectively, taking into account the 2.15 eV band gap energy as shown in the energy band diagram discussed below. Due to the small size of the InN QDs, XPS probes the near-surface band bending of the InGaN layer, which is, hence, significantly altered (reduced) in the presence of the InN QDs. It is this reduction of the band bending which is most important, rather than the precise absolute value[26]. In addition, the electrochemical impedance spectroscopy measurements (Supplementary Note 2) and Mott–Schottky analysis (Supplementary Note 3) presented in Supplementary Figs. 2 and 3 evidence high electrical conductivity and n-type nature of the photoanodes with high carrier density.

Photoelectrochemical properties. The PEC performance of photoanodes A and B was first investigated in three-electrode configuration by linear sweep voltammetry (LSV) in the dark and under white light illumination (100 mW cm^{-2}) at a scan rate of 10 mV s^{-1}. In the three-electrode configuration, the photoanode alone is characterized without the influence of the reaction at the counter electrode. Figure 4 shows the LSV scans for both photoanodes. In the dark, the current densities (green) are negligible in the potential range from −0.7 to 0.8 V versus Ag/AgCl (−0.10–1.41 V versus RHE). Under illumination, the photocurrent densities increase and reach 19.5 mA cm^{-2} at 0.36 V versus Ag/AgCl (0.97 V vs. RHE) for

photoanode A (blue) and 14.4 mA cm^{-2} at 0.68 V vs. Ag/AgCl (1.29 V vs. RHE) for photoanode B (black). The onset potential for photoanode A is −0.2 V vs. Ag/AgCl (0.41 V vs. RHE), clearly smaller than the onset potential for photoanode B. The overall low values of the onset potentials and charge transfer resistance (Supplementary Fig. 2) of photoanodes A and B are due to the favorable valence band maximum position of InGaN below the water oxidation potential. Significant for the present study is the clear lowering of the onset potential due to the QDs. The photocurrent density for a bare Si substrate (brown), for reference, is also shown (likely originating from etching), though the Si surface is not in contact with water during the PEC experiments with the photoanodes A and B.

The PEC performance of the photoanodes was further quantified by illuminating in different wavelength ranges of 380–420 nm, 450–490 nm, 510–550 nm and 630–670 nm with average power density of ~96 mW cm^{-2}. The obtained incident photon-to-current conversion efficiency (IPCE) is plotted in Fig. 5a for photoanode A (blue) and photoanode B (black). The IPCE is the percentage of electrons taking part in the reaction per incident monochromatic photon, according to Eq. (1)[27].

$$IPCE\% = \frac{1240 \times \text{photo current density (mA cm}^{-2})}{\text{Incident light wavelength (nm)} \times \text{light intensity (mW cm}^{-2})} \times 100$$

(1)

The measurements were performed in three-electrode configuration at 0.4 V vs. Ag/AgCl (1.01 V versus RHE) where the photocurrent density is high. The maximum IPCE value for photoanode A is 44% at 530 nm and 29% for photoanode B.
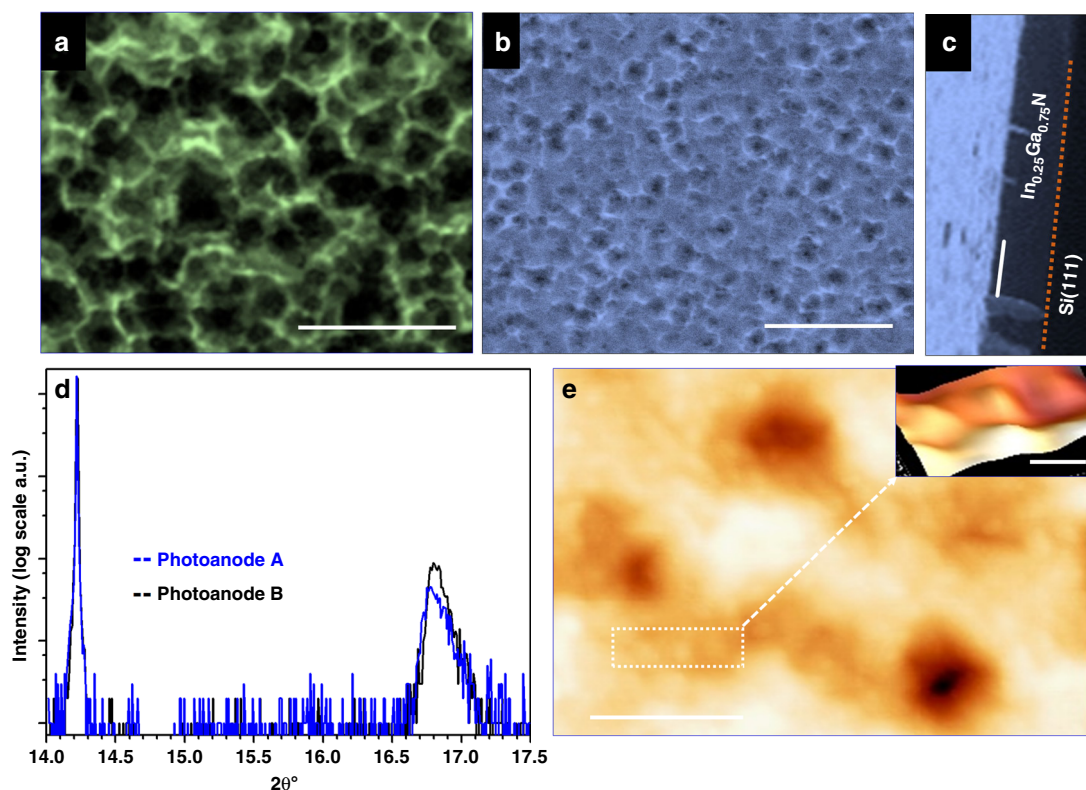

Fig. 1 Morphological and structural characterization of the photoanodes. Top-view SEM images of photoanodes (**a**) A and (**b**) B. **c** Cross-sectional SEM image of photoanode B. The dotted line indicates the InGaN/Si interface. **d** HRXRD ω-2θ spectra of photoanodes A (blue) and B (black) recorded in the vicinity of the Si (111) reflection. **e** AFM height image and (inset) three-dimensional image of the QDs at enlarged magnification of photoanode A. Scale bars are 1 μm in **a** and **b**, 450 nm in **c** and 250 nm in **e** (40 nm in the inset)
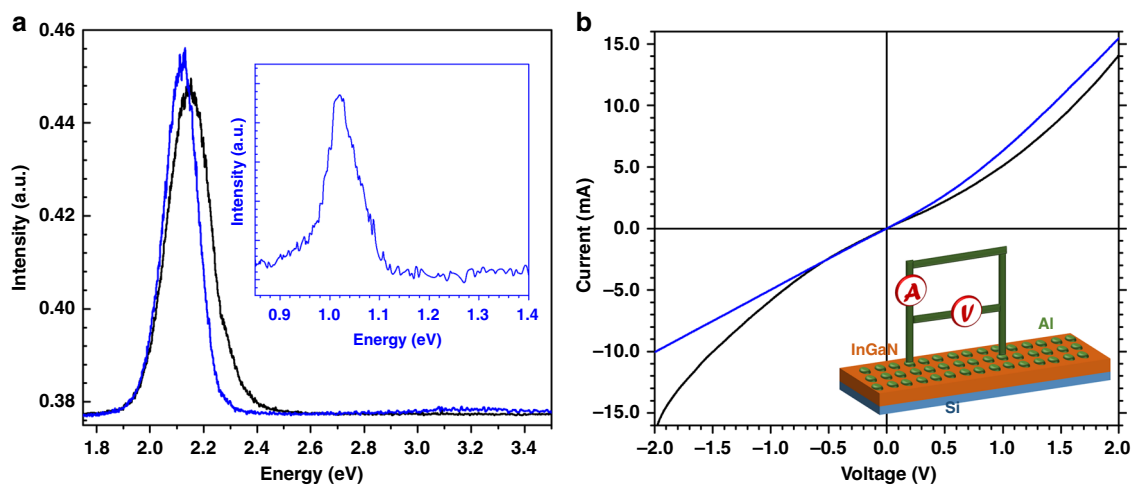
Fig. 2 Optical and electrical characterization of the photoanodes. **a** Low-temperature (17 K) PL spectra of photoanodes A (blue) and B (black). Inset: PL spectrum of photoanode A in the near infra-red range. **b** Two-point I–V measurements for photoanodes A (blue) and B (black). Inset: scheme of the sample structure with I–V measurement setup. The green dots indicate the aluminum contacts on the photoanode
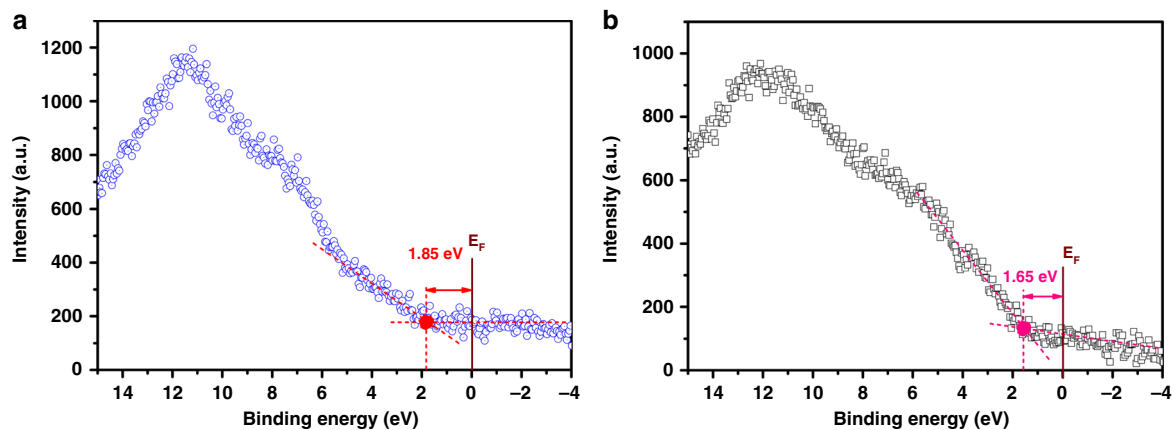

Fig. 3 Near-surface band structure measurements of the photoanodes. XPS valence band spectra of (**a**) photoanode A and (**b**) photoanode B. The spectra are extrapolated, indicated by the red dashed lines, to determine the energy position of the valence band maxima, indicated by the red dots, with respect to the Fermi energy E_F
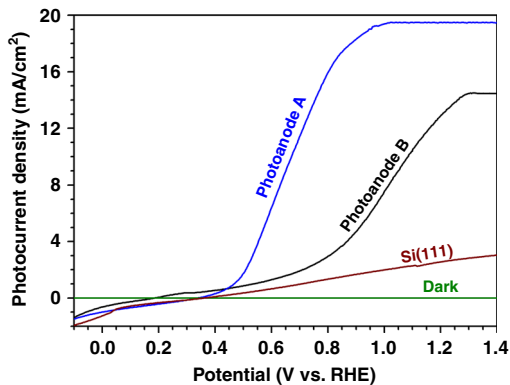

Fig. 4 Photocurrent measurements of the photoanodes. Photocurrent density vs. potential versus RHE of photoanodes A (blue), B (black) and Si (brown) measured in three-electrode configuration under 100 mW cm^{-2} white light illumination. Dark (green) indicates the zero dark currents

The photocurrent density versus time (J–t) transients were measured in two-electrode configuration. This is a true device measurement allowing to determine efficiencies correctly. Figure 5b shows the photocurrent densities for both photoanodes A (blue) and B (black) under white light illumination (100 mW cm^{-2}) with 60 s light on/off cycles for an externally applied bias of 0.2 V vs. the Pt counter electrode. The photocurrent density of photoanode A is approximately four times higher than that of photoanode B, in line with the J–V results. The response time is within 3 s. Most important, the low externally applied bias of 0.2 V leads to a very high photon-to-current efficiency, given in Eq. (2)[28].

$$\eta = \frac{J_p(\text{mA cm}^2)(1.23 - V_{ext})}{l(\text{mW cm}^{-2})} \times 100\%, \qquad (2)$$

where J_p, V_{ext} and l are the photocurrent density, external bias, and illumination power density, respectively, and 1.23 is the redox potential in V. The applied-bias photon-to-current
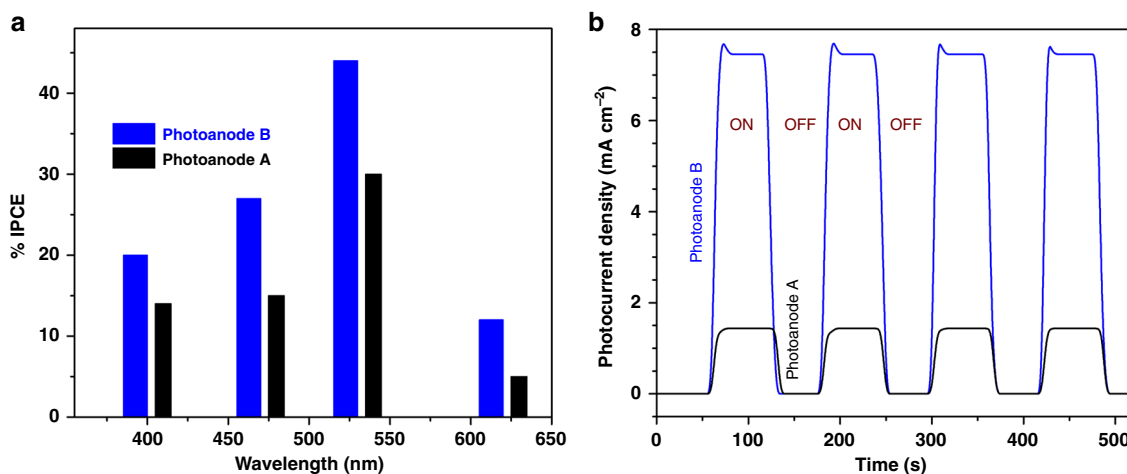
Fig. 5 Efficiency and time response of the photoanodes. **a** IPCE of photoanodes A (blue) and B (black) as function of wavelength measured in three-electrode configuration at 1.01 V versus RHE. **b** Photocurrent densities as function of time measured in two-electrode configuration at 0.2 V versus the Pt counter electrode under 100 mW cm^{-2} white light illumination with 60 s light on/off cycles for photoanodes A (blue) and B (black)
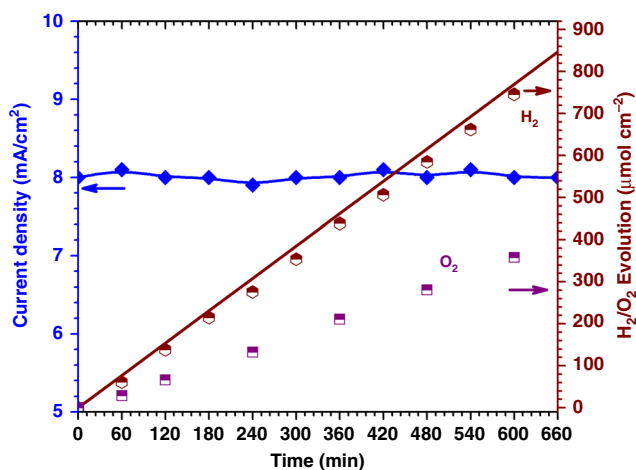

Fig. 6 Quantification of the hydrogen and oxygen gas evolution. Directly measured H$_2$ gas generation (brown/white symbols) as function of time and calculated H$_2$ gas generation (solid brown line) from the photocurrent (blue symbols) measured in two-electrode configuration at 0.2 V vs. the Pt counter electrode for photoanode A under 100 mW cm^{-2} white light illumination. The O$_2$ gas generation (violet/white symbols) is also shown

efficiency reaches 4.1% for photoanode A, compared to 0.78% for photoanode B. This is a more than five times efficiency enhancement due to the QDs.

To confirm the stability of the electrodes and overall water splitting into hydrogen and oxygen gas without other reactions, measurements of the photocurrent density and hydrogen and oxygen gas production were performed over an extended period of time. The measurements were performed in two-electrode configuration under white light illumination at an externally applied bias of 0.2 V versus the Pt counter electrode. The evolved amounts of hydrogen and oxygen are directly quantified using an offline gas chromatography (GC) system (Supplementary Movie 1). In Fig. 6, concentrating on photoanode A, the photocurrent density is indicated on the left-side Y-axis and the hydrogen and oxygen amounts on the right-side Y-axis. During the PEC experiments, we have observed both hydrogen and oxygen evolution (hydrogen evolution at the Pt counter electrode, oxygen evolution at photoanodes A and B). The photocurrent

density (blue symbols in Fig. 6) is very stable over the 10 h with only a small drop. The evolved amount of hydrogen (brown/white symbols in Fig. 6) is compared with the theoretically calculated amount of hydrogen (solid brown line in Fig. 6), according to Faraday's law of electrolysis, given in Eq. (3)[29].

$$\text{Mole of H}_2 = \frac{1}{2}\frac{\int_0^t I \mathrm{d}t}{F},\qquad(3)$$

where F, I and t are are the Faraday constant, measured current and time, respectively. The faradaic efficiency is 87% and the hydrogen generation rate is 75 μmol h^{-1} cm^{-2}. The deviation of the theoretical and experimental values can be related to the offline collection. The measurement of the oxygen amount (violet/white symbols in Fig. 6) gives an oxygen generation rate of 33 μmol h^{-1} cm^{-2}. The slight deviation of the ratio of the oxygen to hydrogen generation rates from 1/2 is again attributed to the off-line collection.

Discussion
The results can be understood by referring to Fig. 7, which shows the energy band diagrams of photoanodes A and B. The directly measured reduction of the upward energy band bending at the surface in the presence of the QDs is a consequence of the well-established high density of intrinsic, positively charged surface donors of InN due to the surface states located in the conduction band[30]. It is the proof of their existence on the InN QD surface to control the near-surface energy band bending of InGaN. These surface donors actively attract electrons or expel holes to catalyze water oxidation, i.e., the oxygen evolution reaction at photoanode A. The QDs do not participate directly in the PEC reaction as their bandgap energy and absorption is too small. The small absorption is due to the small size which in turn, makes the transfer of photogenerated holes directly from the InGaN layer possible, where the absorption takes place without energy relaxation into the (quantized) QD energy levels and this energy relaxation of the holes would inhibit the PEC reaction. The QDs purely act as electrocatalyst for the oxygen evolution reaction.

More precisely, we propose that the positively charged surface donors on the QDs attract/accumulate electrons from the InGaN layer to form an electric dipole (this electron surface accumulation is well characterized for InN layers[30]). It is the corresponding
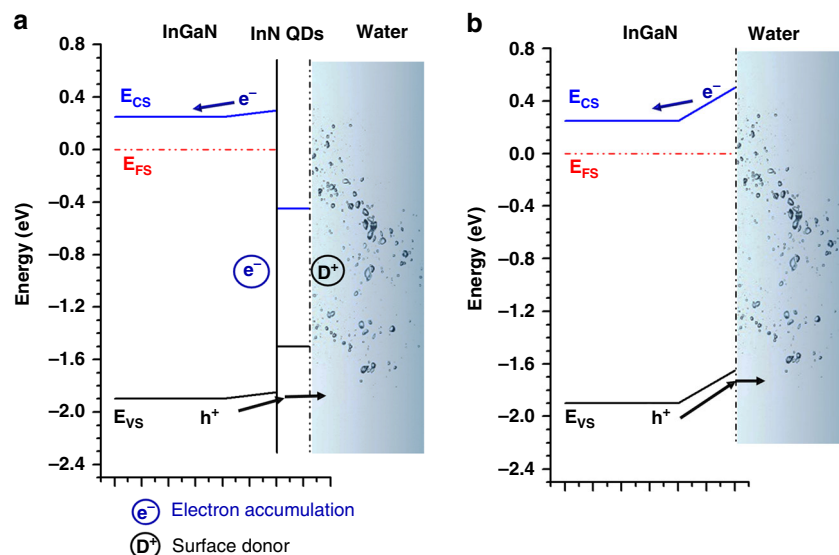
Fig. 7 Energy band structure and PEC reaction scheme of the photoanodes. Schemes of the energy band structure of (**a**) photoanode A and (**b**) photoanode B. E_c indicates the conduction band minimum, E_V indicates the valance band maximum, E_F indicates the Fermi energy, h^+ indicates the photogenerated holes, e^- indicates the photogenerated electrons. The arrows indicate the direction of photogenerated electron and hole transport and the bubbles indicate the O_2 gas generation at the photoanodes due to water oxidation by the photogenerated holes

electric dipole field which catalyzes the water oxidation by attraction of electrons. The presence of the electric dipole field was also documented by the strong attraction of chloride ions for the InN/InGaN QDs operated as ion selective electrode and the strong oxidation enhancement probed by the ferro/ferricyanide redox couple[31,32]. At the same time, the electric dipole field maintains efficient separation of photogenerated electrons and holes in the InGaN layer, despite the reduction of the energy band bending. In addition, the reduced energy band bending facilitates the participation of photogenerated electrons towards proton reduction, i.e., the hydrogen evolution reaction at the Pt counter electrode by reducing the energy barrier for electron transfer. This is relevant for the measurements in two-electrode configuration, probing the full water redox reaction to provide the hydrogen gas production efficiency.

In conclusion, we have revealed the PEC performance for hydrogen generation by water splitting of an InGaN photoanode activated by InN QDs, directly grown on Si (111). The results manifested a more than five-fold enhancement of the overall PEC efficiency for hydrogen evolution for the InN-QDs/InGaN-layer/Si photoanode compared to that for a bare InGaN/Si photoanode. The applied-bias photon-to-current efficiency (4.1%), incident-photon-to-current conversion efficiency (~44%), hydrogen evolution (75 μmol h^{-1} cm^{-2}) and stability of this activated photoanode state or goal to realize efficient photoanodes on cheap Si substrates for cost-effective PEC applications.

Methods

Growth and characterization. All photoanodes were grown in-situ by a plasma-assisted molecular beam epitaxy system (PA-MBE), equipped with a radio-frequency (RF) active nitrogen plasma source. Chemically cleaned 1″ p-type Si (111) substrates (<0.005 Ω cm) were loaded into the introduction chamber, degassed at 500 °C for 4 h and annealed in the growth chamber at 900 °C for 10 min. to desorb the oxide layer from the surface[33,34]. Prior to the growth, the clean Si surface was exposed to the nitrogen plasma at substrate temperature of 850 °C to form a uniform SiN$_x$ layer[35]. This SiN$_x$ layer improves the crystal quality by providing additional pathways for strain relaxation. The optimized nitrogen, Ga and In fluxes for InGaN growth were 9, 5.4 and 2.5 nm min^{-1}, respectively. The substrate temperature was 450 °C. The relatively low substrate temperature kinetically suppresses phase separation, while the close-to-stoichiometric, slightly nitrogen rich N-to-In + Ga flux ratio supports the growth of a compact layer. The final layer thickness was 450 nm. The InN QDs were grown via the Stranski–Krastanov mode using the same nitrogen and In fluxes and growth

temperature for 2 min. without Ga flux. All samples were characterized *ex-situ* for their morphological (field emission scanning electron microscopy (FESEM) and atomic force microscopy (AFM)), structural (high-resolution X-ray diffraction (HRXRD)), optical (low-temperature photoluminescence (LT-PL)), electronic (X-ray photoelectron spectroscopy (XPS)) and electrical (current-voltage (I–V) measurements) properties. High-resolution transmission electron microscopy (HR-TEM) measurements of the InN QDs, InGaN layer and InGaN/SiN$_x$/Si interface have been reported previously[34,36].

Photoelectrochemical measurements. The PEC experiments were performed using a three-electrode setup with InGaN working electrode, Pt counter electrode and Ag/AgCl reference electrode immersed in 0.1 M Na$_2$SO$_4$/H$_2$SO$_4$ (pH = 7.0) aqueous electrolyte solution. This electrolyte has been used before and is stable for the applied voltages. For the working electrodes, the InGaN samples were cut into rectangular pieces with an active area of 0.125 cm^2. Ohmic contacts were made using evaporated Al, silver paste and Cu wires, covered by insulating epoxy. A 100 mW cm^{-2} Xenon arc lamp (white light with 1-sun power density), together with various optical filters for spectrally resolved measurements, was used for illumination. The PEC chamber was air cooled, keeping the electrolyte temperature at 25 °C. An electrochemical workstation (Metrohm 304) was used throughout this study.

Direct gas detection was performed by an Agilent 7890 A GC system equipped with a thermal conductivity detector and a high performance 5 Å molecular sieve packed column, which was held isothermally at 50 °C. Pure Argon was used as carrier gas at a flow rate of 19.3 mL/min. At the desired time, 1 mL of the sample gas from the 50 mL reaction vessel was collected in 1.5 mL of glass syringe and manually injected into the GC system for analysis. Before sample gas measurements, the instrument was calibrated with H$_2$ and O$_2$ gas standards under the same conditions.

Data availability

The authors declare that the main data supporting the findings of this study are available within the paper and its Supplementary Information file. Other relevant data are available from the corresponding author upon reasonable request.

References

1. Qu, Y. & Duan, X. Progress, challenge and perspective of heterogeneous photocatalysts. *Chem. Soc. Rev.* **42**, 2568–2580 (2013).
2. Hisatomi, T. & Domen, K. Introductory lecture: sunlight-driven water splitting and carbon dioxide reduction by heterogeneous semiconductor systems as key processes in artificial photosynthesis. *Faraday Discuss.* **198**, 11–35 (2017).

3. Jia, J. et al. Solar water splitting by photovoltaic-electrolysis with a solar-to-hydrogen efficiency over 30%. *Nat. Commun.* **7**, 13237 (2016).

4. May, M. M., Lewerenz, H. J., Lackner, D., Dimroth, F. & Hannappel, T. Efficient direct solar-to-hydrogen conversion by in-situ interface transformation of a tandem structure. *Nat. Commun.* **6**, 8286 (2015).

5. Montoya, J. H. et al. Materials for solar fuels and chemicals. *Nat. Mater.* **16**, 70–81 (2017).

6. Jiang, C., Moniz, S. J. A., Wang, A., Zhang, T. & Tang, J. Photoelectrochemical devices for solar water splitting – materials and challenges. *Chem. Soc. Rev.* **46**, 4645–4660 (2017).

7. Bae, D., Seger, B., Vesborg, P. C. K., Hansen, O. & Chorkendorff, L. B. Strategies for stable water splitting via protected photoelectrodes. *Chem. Soc. Rev.* **46**, 1933–1954 (2017).

8. Young, J. L. et al. Direct solar-to-hydrogen conversion via inverted metamorphic multi-junction semiconductor architectures. *Nat. Energy* **2**, 17028 (2017).

9. Cho, I. S. et al. Co-doping titanium dioxide nanowires with tungsten and carbon for enhanced photoelectrochemical performance. *Nat. Commun.* **4**, 1723 (2013).

10. Chen, X. et al. Recent advances in visible-light-driven photoelectrochemical water splitting: catalyst nanostructures and reaction systems. *Nano Micro Lett.* **8**, 1–12 (2016).

11. Luo, J. et al. Homogeneous photosensitization of complex TiO_2 nanostructures for efficient solar energy conversion. *Sci. Rep.* **2**, 451 (2012).

12. Wood, B. C., Schwegler, E., Choi, W. I. & Ogitsu, T. Surface chemistry of GaP (001) and InP(001) in contact with water. *J. Phys. Chem. C* **118**, 1062–1070 (2014).

13. Kibria, M. G. & Mi, Z. Artificial photosynthesis using metal/nonmetal-nitride semiconductors: current status, prospects, and challenges. *J. Mater. Chem.* **A4**, 2801–2820 (2016).

14. Alvi, N. H. et al. InN/InGaN quantum dot photoelectrode: efficient hydrogen generation by water splitting at zero voltage. *Nano Energy* **13**, 291–297 (2015).

15. Chowdhury, F. A., Trudeau, M. L., Guo, H. & Mi, Z. A photochemical diode artificial photosynthesis system for unassisted high efficiency overall pure water splitting. *Nat. Commun.* **9**, 1707 (2018).

16. Ebaid, M. et al. Water splitting to hydrogen over epitaxially grown InGaN nanowires on a metallic titanium/silicon template: reduced interfacial transfer resistance and improved stability to hydrogen. *J. Mater. Chem. A.* **6**, 6922–6930 (2018).

17. Liu, H. et al. Controllable synthesis of $[11\overline{2}\overline{2}]$ faceted InN nanopyramids on ZnO for photoelectrochemical water splitting. *Small* **14**, 1703623 (2018).

18. Butson, J. et al. Photoelectrochemical studies of InGaN/GaN MQW photoanodes. *Nanotechnology* **29**, 045403 (2018).

19. AlOtaibi, B. et al. Highly stable photoelectrochemical water splitting and hydrogen generation using a double-band InGaN/GaN core/shell nanowire photoanode. *Nano Lett.* **13**, 4356–4361 (2013).

20. Park, J. H. et al. Hydrogen generation using non-polar coaxial InGaN/GaN multiple quantum well structure formed on hollow n-GaN nanowires. *Sci. Rep.* **6**, 31996 (2016).

21. Fan, S., Woo, S. Y., Vanka, S., Botton, G. A. & Mi, Z. An $In_{0.5}Ga_{0.5}N$ nanowire photoanode for harvesting deep visible light photons. *APL Mater.* **4**, 076106 (2016).

22. Kibria, M. G. et al. Tuning the surface Fermi level on p-type gallium nitride nanowires for efficient overall water splitting. *Nat. Commun.* **5**, 3825 (2014).

23. Aseev, P. et al. Uniform low-to-high In composition InGaN layers grown on Si. *Appl. Phys. Express* **6**, 115503 (2013).

24. Moret, M. et al. Optical, structural investigations and band-gap bowing parameter of GaInN alloys. *J. Cryst. Growth* **311**, 2795–2797 (2009).

25. Wagner, C. D., Riggs, W. M., Davis, L. E., Moulder, J. F. & Muilenberg, G. E. *Handbook of X-Ray Photoelectron Spectroscopy* (Perkin Elmer Corp., United States of America, 1979).

26. Veal, T. D. et al. Transition from electron accumulation to depletion at InGaN surfaces. *Appl. Phys. Lett.* **89**, 202110 (2006).

27. Gratzel, M. Photoelectrochemical cells. *Nature* **414**, 338 (2001).

28. Shi, X. et al. Unassisted photoelectrochemical water splitting exceeding 7% solar-to-hydrogen conversion efficiency using photon recycling. *Nat. Commun.* **7**, 11943 (2016).

29. Shin, S. M., Jung, J. Y., Park, M. J., Song, J. W. & Lee, J. H. Catalyst-free hydrogen evolution of Si photocathode by thermovoltage-driven solar water splitting. *J. Power Sources* **279**, 151–156 (2015).

30. King, P. D. C. et al. Variation of band bending at the surface of Mg-doped InGaN: evidence of p-type conductivity across the composition range. *Phys. Rev. B* **75**, 115312 (2007).

31. Alvi, N. H. et al. Highly sensitive and fast anion-selective InN quantum dot electrochemical sensors. *Appl. Phys. Express* **6**, 115201 (2013).

32. Soto Rodriguez, P. E. D. et al. Electrocatalytic oxidation enhancement of InGaN films and nanostructures grown directly on Si(111). *Electrochem. Commun.* **60**, 158–162 (2015).

33. Kumar, P. et al. First demonstration of direct growth of planar high-In-composition InGaN layers on Si. *Appl. Phys. Express* **6**, 035501 (2013).

34. Soto Rodriguez, P. E. D. et al. Stranski-Krastanov InN/InGaN quantum dots grown directly on Si(111). *Appl. Phys. Lett.* **106**, 023105 (2015).

35. Kumar, P., Tuteja, M., Kesaria, M., Waghmare, U. V. & Shivaprasad, S. M. Superstructure of self-aligned hexagonal nanorods of GaN on nitrided Si(111) surface. *Appl. Phys. Lett.* **101**, 131605 (2012).

36. Soto Rodriguez, P. E. D. et al. Spontaneous formation of InGaN nanowall network directly on p-Si(111). *Appl. Phys. Lett.* **102**, 173105 (2013).

Acknowledgements

Author contributions

P.K. P.D. conceived the idea and conducted the experimental work. The photoanodes were grown and characterized by P.K. PEC experiments were performed by P.D. and P.K. X.P.S. analysis was completed by P.K. and S.M.S. R.N., R.K.S., G.Z. and S.M.S. were the part of the discussion to technically understand the results. R.N. has helped in understanding the PEC results. R.J. has helped during experiments. P.K. & P.D. has drafted the manuscript. All authors have discussed and commented on the manuscript.

Additional information